1 GNSS-corrected InSAR Displacement Time Series Spanning the 2019

2 Ridgecrest, CA Earthquakes

Katherine Guns^{1†}, Xiaohua Xu², Yehuda Bock¹, and David Sandwell¹ ¹Institute of Geophysics and Planetary Physics, Scripps Institution of Oceanography, University of California, San Diego, La Jolla, CA, 92093-0225 ²Institute for Geophysics, University of Texas at Austin, Austin, TX, 78758 [†]Corresponding Author: Katherine Guns kguns@ucsd.edu Date Submitted: September 21, 2021 Abbreviated Title for page heading: Ridgecrest-Spanning InSAR Time Series

31 **Summary** 32 InSAR displacement time series are emerging as a valuable product to study a number of earth 33 processes. One challenge to current time series processing methods, however, is that when large 34 earthquakes occur, they can leave sharp coseismic steps in the time series. These discontinuities 35 can cause current atmospheric correction and noise smoothing algorithms to break down, as 36 these algorithms commonly assume that deformation is steady through time. Here, we aim to 37 remedy this by exploring two methods for correcting earthquake offsets in InSAR time series: a 38 Simple Difference Offset Estimate (SDOE) process and a Multiparameter Offset Estimate 39 (MPOE) parametric time series inversion technique. We apply these methods to a two-year time 40 series of Sentinel-1 interferograms spanning the 2019 Ridgecrest, CA earthquake sequence. 41 Descending track results indicate that the SDOE method precisely corrects for only 20% of the 42 coseismic offsets at 62 study locations included in our scene and only partially corrects or 43 sometimes overcorrects for the rest of our study sites. On the other hand, the MPOE estimate 44 method successfully corrects the coseismic offset for the majority of sites in our analysis. This 45 MPOE method allows us to produce InSAR time series and data-derived estimates of 46 deformation during each phase of the earthquake cycle. In order to better isolate and estimate the 47 signal of postseismic lithospheric deformation in the InSAR time series, we apply a GNSS-based 48 correction to our interferograms. This correction ties the interferograms to median-filtered 49 weekly GNSS displacements and removes additional atmospheric artifacts. We present InSAR-50 based estimates of postseismic deformation for the area around the Ridgecrest rupture, as well as 51 a two-year coseismic-corrected, GNSS-corrected InSAR time series dataset. This GNSS-52 corrected InSAR time series will enable future modeling of postseismic processes such as 53 afterslip in the near field of the rupture, poroelastic deformation at intermediate distances, and 54 viscoelastic deformation at longer time scales in the far field. 55 56 **Keywords:** Satellite geodesy, Seismic cycle, Transient deformation, Time-series analysis, North 57 America 58

59

60

61

1. Introduction

62

63 The rise of high precision, satellite-based geodetic measurements over the last three decades has 64 allowed us to better understand the Earth system in a variety of ways (Burgmann & Thatcher, 65 2013; Bock & Melgar, 2016; Biggs & Wright, 2020). Using both Global Navigation Satellite System (GNSS) and Synthetic Aperture Radar (SAR) observations of the surface, we can 66 67 quantify hydrologic loading processes in the hydrosphere and cryosphere (e.g., Argus et al. 68 2005; Chaussard et al. 2014; Neely et al. 2021; Bock & Wdowinski, 2021), magmatic processes 69 at active volcanic centers (e.g., Berardino et al. 2002; Poland et al. 2006), landslide processes 70 (e.g., Hilley et al. 2004; Tong & Schmidt, 2016; Handwerger et al. 2019; Bekaert et al. 2020; Hu 71 et al., 2020), and earthquake cycle processes (e.g., Bürgmann et al. 2000; Wei et al. 2011; Weiss 72 et al. 2020; Xu et al. 2021) with continually improving temporal and spatial resolution. For SAR 73 methods in particular, the ongoing European Space Agency Copernicus Sentinel-1 mission 74 provides open-access data with excellent coverage around the globe at increased temporal 75 resolution compared to previous missions. This reliable dataset of SAR images, in combination 76 with improved processing strategies for Interferometric SAR (InSAR), has enabled the 77 production of precise displacement time series, which are proving to be an invaluable tool for 78 assessing deformation over time (Hooper et al. 2012). Some researchers calculate long-term 79 average velocities from InSAR time series in order to analyze different deformation signals (e.g., 80 Bürgmann et al. 2005; Dixon et al. 2006; Weiss et al. 2020), while others rely on the 81 displacement over time to illuminate the temporal evolution of a particular process (Hetland et 82 al. 2012; Chaussard et al. 2014; Xu et al. 2018; Tymofyeyeva et al. 2019; Klein et al. 2019). 83 Due to high spatial resolution, InSAR time series can sharpen the picture of interseismic 84 deformation and fault creep, as GNSS motions, even in areas of close station spacing, are not as 85 effective at illuminating discontinuities in surface displacements across faults (Tong et al. 2013; 86 Shirzaei & Bürgmann, 2013; Fattahi & Amelung, 2016). 87 88 Processing InSAR time series often relies on a fundamental assumption that all deformation 89 present in the time series is relatively steady over time. This assumption enables the effective 90 correction of atmospheric errors and other noise sources (Tymofyeyeva & Fialko, 2015; Xu et al. 91 2017). A seismic event that is large enough to register displacement at the surface however, 92 introduces an abrupt step into the time series, which then causes time series processing and

93 smoothing algorithms to break down. Some researchers even use these abrupt steps in pixel time 94 series to search for smaller and less conspicuous earthquakes in interferograms (e.g., Grandin et 95 al. 2017; Liu et al. 2021). Hetland et al. (2012) have developed a computer code to explicitly 96 deal with earthquake offsets and other time-dependent processes (known as MInTS). Here we 97 refine their approach with application to the July 2019 Ridgecrest earthquakes. 98 99 The July 4th, 2019 M_W 6.4 and July 5th, 2019 M_W 7.1 Ridgecrest earthquakes ruptured a 100 previously unmapped series of faults (e.g., Ponti et al. 2020) in the eastern California Mojave 101 desert (Fig. 1), and was one of the most well-observed earthquake sequences in recent history. 102 These events allowed the active tectonics community a detailed firsthand look at a number of 103 earthquake processes, including postseismic deformation (viscoelastic relaxation, afterslip, and 104 poroelastic effects; e.g., Wang & Bürgmann, 2020), aftershock patterns (e.g., Hardebeck, 2020), 105 mechanical fault structure and behavior in the rupture zone (e.g., Plesch et al. 2020; Xu et al. 106 2020a,b; Milliner et al. 2021), and possible impact on nearby fault zones (e.g., Ross et al. 2019). 107 In addition, the location of these earthquakes has favorable conditions for InSAR analysis, 108 including an arid climate and a high coherence desert landscape lacking in vegetation. 109 110 To best estimate the coseismic offset introduced by the Ridgecrest earthquake sequence, we 111 explore two methods to estimate coseismic displacements within InSAR time series: (1) a 112 straightforward Simple Difference Offset Estimate (SDOE) approach and (2) a Multiparameter 113 Offset Estimate (MPOE) time series estimate approach. We additionally use our coseismic-114 corrected time series to calculate an estimate of the cumulative postseismic deformation 115 following the two mainshock events. To further improve our estimates of postseismic 116 deformation, we use the dense network of GNSS stations in the area to incorporate a GNSS-117 based correction to our InSAR time series. This correction mainly helps mitigate large spatial-118 scale (long wavelength) atmospheric errors, but also helps provide an underlying spatial 119 reference for the InSAR deformation. When used together, InSAR and GNSS displacement time 120 series can better illuminate ongoing processes than either dataset alone, and we create a final 121 product of GNSS-corrected, coseismic-corrected InSAR time series. In addition, by utilizing our 122 MPOE time series estimate method, we produce a series of map-view earthquake cycle products that delineate the interseismic, coseismic, and postseismic periods of the earthquake cycle from InSAR time series.



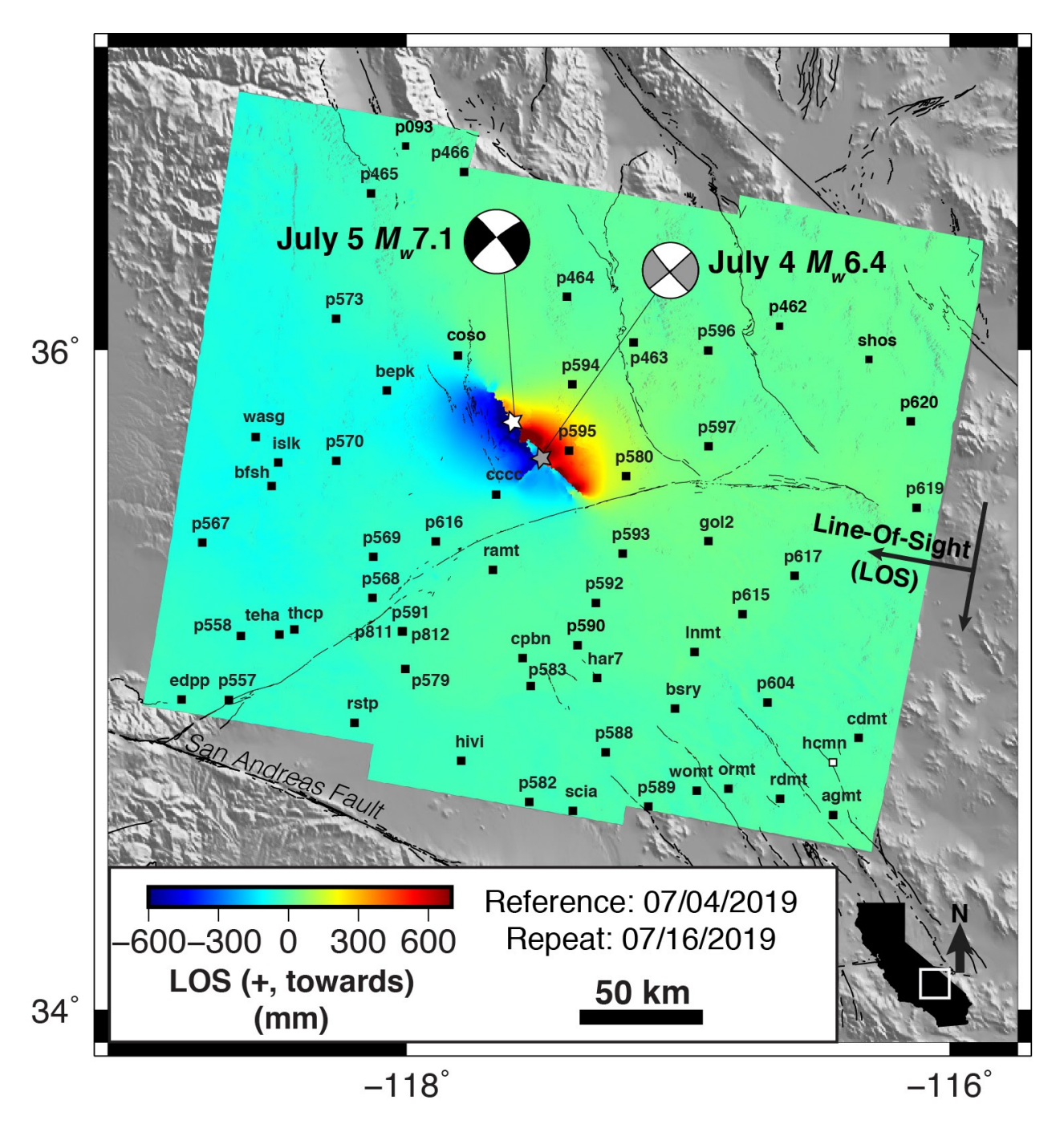


Figure 1. Unwrapped descending track 071 Sentinel-1 interferogram illustrating the coseismic and early postseismic displacements of the July 2019 Ridgecrest earthquake sequence in satellite Line-Of-Sight (LOS), where red (positive) means motion towards the satellite. Locations of GNSS stations labeled by

their 4-character station codes. In future plots we reference interferograms to the location of station HCMN (white square, lower right). Focal mechanism nodal planes from USGS Earthquake catalog.

2. Methods

2.1 InSAR Processing

To incorporate the displacements introduced by the Ridgecrest sequence into InSAR time series analyses, we start by processing 90 descending track images through the time period of July 2018 to July 2020, and 79 ascending track images through the time period of November 2018 to July 2020, all with repeat times between 6 and 12 days. We center our analysis on scenes that cover the area around the Ridgecrest rupture, which were collected by the C-Band Sentinel-1 satellites operating in Terrain Observation by Progressive Scan (TOPS) mode across descending track 71 and ascending track 64. We download Single Look Complex (SLC) data files from the Alaska Satellite Facility and process them using GMTSAR version 6.1 (Sandwell *et al.* 2016) and begin by aligning all secondary scenes to a single reference image chosen through visual inspection of a perpendicular baseline-versus-time plot (**Fig. S1**). This coregistration process is described in detail by Xu et al. (2017) and takes a geometric approach that increases the accuracy of pixel alignment and improves phase recovery.

We calculate interferograms for each of the three TOPS subswaths of the aligned set of images, and then merge the products in radar coordinates to create a full scene interferogram for each day pair that falls within a \leq 50-day temporal baseline and a \leq 100-m spatial perpendicular baseline and low-pass filter them at 200 m wavelength. Once we have our merged interferograms, we unwrap the phase of each pair using the Statistical-Cost, Network-Flow Algorithm for PHase Unwrapping (SNAPHU) program (Chen & Zebker, 2002; Agram & Zebker, 2009) implemented within the GMTSAR package. We apply a large phase discontinuity threshold to allow for the displacements observed during the Ridgecrest sequence. To remove areas of poor coherence from the unwrapping process, we create a mask of common points of poor coherence throughout our stack of interferograms that excludes small areas in the neighboring Sierra Nevada and Central Valley (mainly bodies of water and areas of snow cover and agriculture). This process produces a set of 415 descending track unwrapped interferograms and 389 ascending track unwrapped interferograms showing

161 coseismic motion is presented in Fig. 1, and is formed from the closest pair of images to 162 encompass the Ridgecrest earthquake sequence, July 4th, 2019 and July 16th, 2019. In this study, 163 we primarily focus our analysis on the descending track interferograms due to the lower levels of 164 noise present in the data collected in the morning (versus the ascending track which is collected 165 in the late afternoon). 166 167 2.2 Time Series Processing 168 For calculating a time series from our unwrapped interferograms, we use the coherence-based 169 Small Baseline Subset (SBAS) approach (Berardino et al. 2002; Schmidt & Bürgmann, 2003; 170 Tymofyeyeva & Fialko, 2015; Tong & Schmidt, 2016; Xu et al. 2017; Xu et al. 2021) 171 implemented within GMTSAR. This SBAS approach takes in coherence values of the 172 interferograms as weights in a least-squares inversion for time series at every pixel, instead of 173 removing low-coherence pixels altogether (Xu et al. 2017). To prepare for SBAS processing we 174 further downsample unwrapped interferograms to 32 pixels in range (32 pixel spacing using a 175 bicubic interpolation in GMT) and 8 pixels in azimuth (8 pixel spacing using a bicubic 176 interpolation in GMT) to save storage space and computation time, and reference our descending 177 track interferograms to a stable reference point located >120 km southeast of the Ridgecrest 178 rupture zone at the location of continuous GNSS station HCMN (see white square in Fig. 1). 179 180 The first step we take is to run SBAS for our interferograms with no temporal smoothing or 181 correction parameters. This produces a displacement time series in Line of Sight (LOS) that 182 includes both the discontinuous coseismic offset from the Ridgecrest earthquake sequence, as 183 well as the postseismic deformation that followed the main event (Fig. 2). A common next step 184 in calculating InSAR time series with SBAS is to apply a temporal smoothing constraint (e.g., 185 Schmidt & Bürgmann, 2003), which has been shown to successfully reduce noise and correct for 186 propagation delays through the troposphere and the ionosphere using a Common-scene Stacking 187 (CSS) approach (Tymofyeyeva & Fialko, 2015; Xu et al. 2017). Both the CSS correction and 188 any chosen smoothing constraint however, include a primary assumption that all displacements 189 in the time series are steady over the time span of observation of the series. To illustrate the 190 adverse effects of applying this correction we apply it to our set of interferograms. The effect of

temporal smoothing and the CSS correction across the sharp coseismic step is immediately

apparent (**Fig. 2B**). The correction spreads the sharp displacement jump across more than fifteen displacement time steps, which does not accurately capture the deformation caused by the earthquake rupture. Thus, to properly apply any smoothing constraints, we will first need to remove the coseismic displacement.

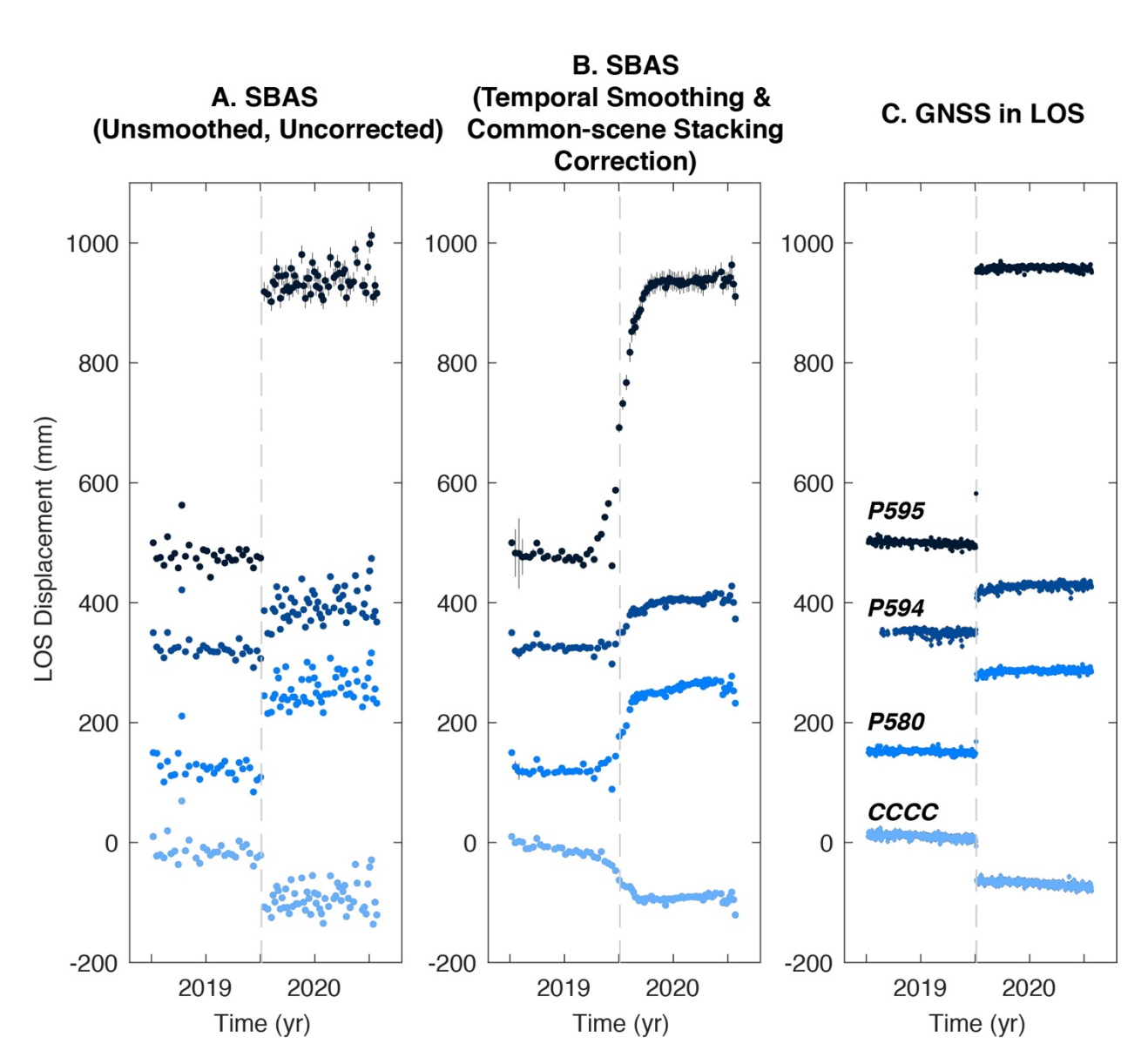


Figure 2. InSAR time series at the locations of four GNSS stations near the Ridgecrest rupture produced through the Small Baseline Subset (SBAS) method with (A) no temporal smoothing or correction, (B) temporal smoothing and the CSS correction applied; (C) GNSS time series in Line-of-Sight (LOS) for comparison. Uncertainties for InSAR time series calculated as a standard deviation of a 10x10 pixel area around the station location point. Grey dashed lines represent the occurrence of the Ridgecrest earthquake sequence.

2.3 Estimating Time Series Motions

206

207

2.3.1 GNSS Time Series

- 208 To quantify long term velocities and postseismic displacements for specific locations across our
- 209 InSAR scenes for comparison between InSAR and GNSS displacement time series, we apply a
- 210 parametric time series model commonly used in GNSS time series processing (Nikolaidis, 2002;
- Bevis & Brown, 2014; Bock & Melgar, 2016). We start by using the Extended Solid Earth
- 212 Science ESDR System (ESESES) daily Combination time series (Clean Weighted Mean
- 213 Combination, removed of non-tectonic offsets, 08/10/2021 Solution) (http://sopac-
- 214 csrc.ucsd.edu/index.php/displacements/) produced as part of NASA's Making Earth System Data
- 215 Records for Use in Research Environments (MEaSUREs) program (Bock et al. 2021). The
- 216 combination time series are estimated from independent analyses of the GNSS data by Scripps
- 217 Institution of Oceanography and Jet Propulsion Laboratory using a common source of metadata.
- We crop the GNSS time series to the time period of our InSAR time series (2018.5000 to
- 219 2020.5000) and project the time series observations for each station into LOS. We then use a
- least squares inversion, weighted by the LOS-projected GNSS uncertainties, to estimate our
- parametric terms as follows:

222

223
$$D(t) = A_1 + A_2 * t + A_3 \sin(2T_1t) + A_4 \cos(2T_1t) + A_5 \sin(2T_{0.5}t) + A_6 \cos(2T_{0.5}t)$$

$$+ \left[A_7 * H(t - t_{M6.4eq}) \right] + \left[A_8 * H(t - t_{M7.1eq}) \right] + \left[A_9 \left(1 - e^{-\frac{\Delta t}{\tau}} \right) * H(t - t_{eq}) \right]$$
 [1]

- where D(t) represents total displacements present at a given time t, and $H(t t_{eq})$ is the
- Heaviside function, where t_{eq} is equal to the respective time (in decimal year) of the $M_W6.4$ or
- 228 M_W 7.1 event. Numbered parameters correspond to initial position (A_1) , velocity (A_2) , seasonal
- terms for annual ($T_1 = 1$ year) and semiannual ($T_{0.5} = \frac{1}{2}$ year) periods ($A_3 A_6$), the Ridgecrest
- coseismic offsets $(A_7 A_8)$, and an exponential postseismic term for the Ridgecrest earthquake
- sequence (A_9) using a characteristic relaxation time (τ) of 182.5 days (half year). These terms are
- the same terms solved for in the MEaSUREs time series analysis of daily displacement. LOS-
- projected GNSS station displacements and their final models are presented in Fig. S2 for ten

representative stations. We use the estimated exponential term amplitude from the model to calculate a cumulative postseismic displacement over the two months directly following the earthquake sequence (see **Table 1**).

2.3.2 InSAR Time Series for Individual Pixels

When we estimate a time series model from the SBAS-produced InSAR time series for any given pixel, we apply an approach similar to that of Hetland et al. (2012) and Neely et al. (2021) that estimates similar model terms to the GNSS time series parametric model in [1]:

 $D(t) = A_1 + A_2 * t + \left[A_3 * H(t - t_{eq}) \right] + \left[A_4 \left(1 - e^{-\frac{\Delta t}{\tau}} \right) * H(t - t_{eq}) \right]$ [2]

For the InSAR time series however, we make three adjustments to equation [1] to produce equation [2]: (1) estimate only a single combined coseismic offset for both main Ridgecrest events instead of two (given the lack of temporal resolution for InSAR scenes compared to daily GNSS solutions); (2) we do not estimate seasonal terms on InSAR time series due to both the short 2-year time span of our time series and the high levels of noise, as the seasonal term can then further bias the coseismic offset estimate; and (3) we use a non-weighted least squares solution to estimate the final model terms. The non-weighted framework here is due to the lack of accurate estimated uncertainties for each pixel, a challenge that is an active area of research (e.g., Tong *et al.* 2013; Agram & Simons, 2015). Estimating a time series model is our primary means of constraining each deformation phase in the earthquake cycle directly from the InSAR time series, which we compare with estimates from the GNSS time series.

2.4 Incorporating Coseismic Displacement

2.4.1 Simple Difference Offset Estimate (SDOE) Correction

In order to account for the coseismic offset caused by the earthquake events, we first calculate an unsmoothed SBAS time series for the set of interferograms, resulting in a sharp step in interferograms spanning the earthquakes as shown in **Fig. 2A**. We isolate the deformation primarily caused by the coseismic rupture by subtracting the first SBAS-produced displacement grid after the earthquake from the displacement grid just before the earthquakes to create a

gridded coseismic estimate, or our SDOE grid (**Fig. 3A**). This is the simplest way to estimate the coseismic offset, and is computationally quick and efficient. This resulting grid is then subtracted from all interferograms pairs that span the earthquakes (**Fig. 3A**). We then run SBAS using all the original downsampled interferograms, but with the replacement of the ten earthquake-spanning interferograms that have the SDOE estimate grids removed. Since postseismic displacements, which gradually decay with time, are small compared to the coseismic displacements for the Ridgecrest earthquake sequence (Jin & Fialko, 2020), we can then apply the CSS correction to this time series dataset in order to reduce the levels of noise from atmospheric propagation delay (Tymofyeyeva & Fialko, 2015). Applying the CSS correction has been successful for seasonal signals (Tymofyeyeva & Fialko, 2015), which vary over time scales that are smaller than the decaying exponential signal of a postseismic signal. The results of this approach are illustrated in **Fig. 4A** for four different stations near the Ridgecrest rupture.

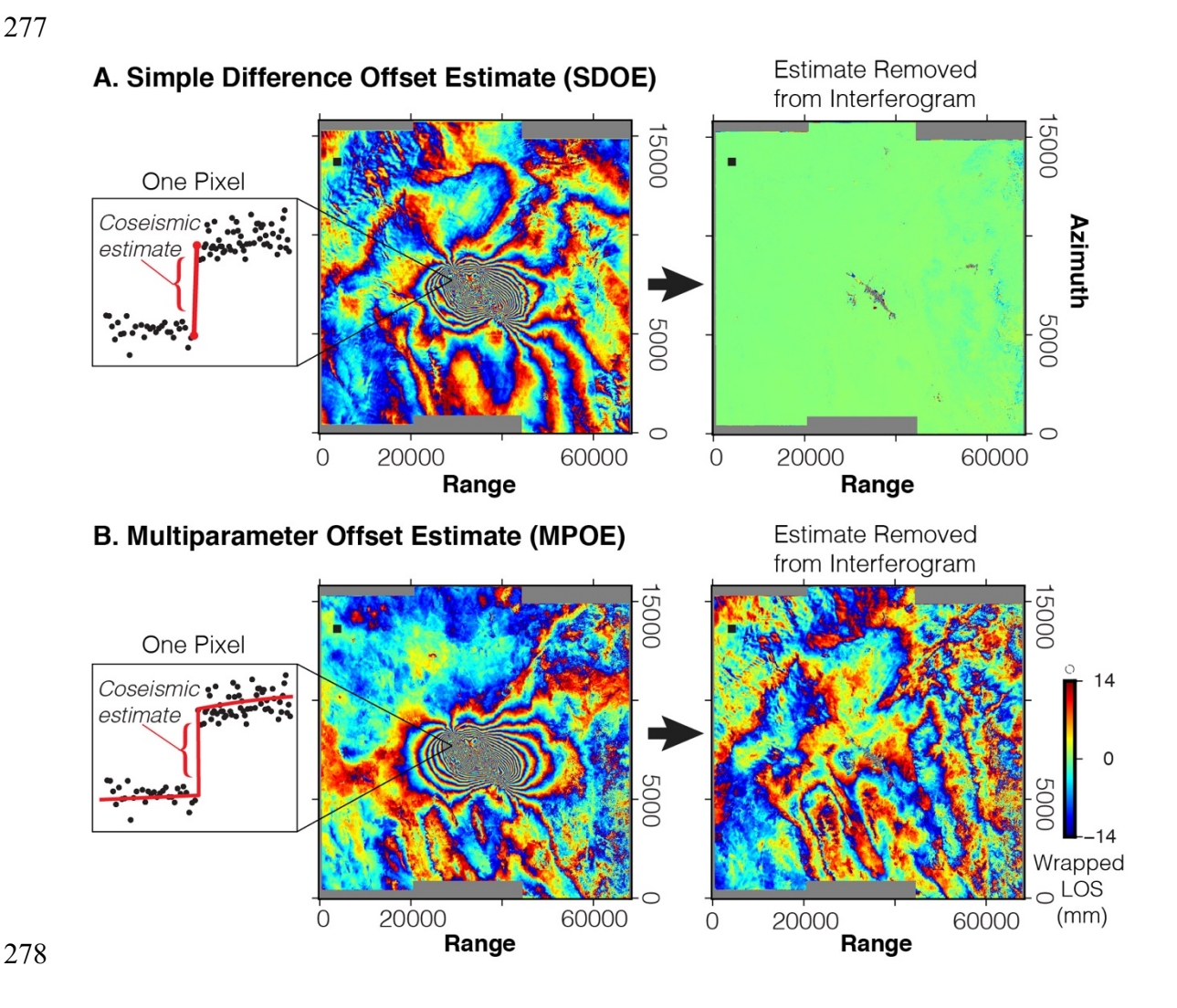


Figure 3. Two trial methods of correcting the coseismic displacement from the Ridgecrest earthquake sequence, presented in radar coordinates; (A) shows our Simple Difference Offset Estimate (SDOE) calculated by differencing the SBAS-produced displacement grids bracketing the earthquake, and the result of subtracting that estimate grid from the descending 07/04/2019—07/16/2019 coseismic interferogram while (B) shows our Multiparameter Offset Estimate (MPOE) grid calculated through a pixel-by-pixel time series estimation process, as well as the result of subtracting this MPOE estimate from the interferogram. The MPOE correction removes the coseismic signal and leaves behind the noise, while the SDOE correction removes both coseismic signal and noise, which can then lead to artificial overcorrections of the coseismic offset. Black square is the reference point.

2.4.2 Multiparameter Offset Estimate (MPOE) Correction

Our second coseismic correction test case implements a Multiparameter Offset Estimate (MPOE) correction. We calculate this correction grid by estimating a parametric time series model (using equation [2] of Section 2.3.2) for each pixel's time series from an SBAS-produced InSAR displacement grid set using an approach similar to Hetland et al. (2012), but using only a leastsquares inversion instead of wavelet decomposition analysis. This parametric model estimates an initial position, a velocity, an exponential postseismic term with a relaxation time (τ) value of a half year, and, most importantly, a coseismic offset. This approach allows us to estimate the coseismic offset using the entire InSAR time series (N = 71 epochs) rather than just the single time epoch before and single time epoch after the events, and thus is able to suppress noise more effectively; however, it requires a more complex coding approach and takes more time to compute. Similar methods, including fitting a line to a groups of displacement epochs just before and just after the event, could also improve the resolvability for smaller events (e.g., Liu et al. 2021). Once we have a coseismic estimate for every grid pixel, we remove that MPOE grid from each of our ten earthquake-spanning interferograms (Fig. 3B). We then run another SBAS to calculate MPOE coseismic-corrected time series displacement grids. The results of this approach are illustrated in Fig. 4B.

3. Results

To determine which of our two coseismic correction methods produces the best result using the descending track time series dataset, we compare the coseismic offsets estimated using our time series analysis (section 2.3.2) before the correction and after the correction, for the 62 specific

pixels that correspond to the locations of GNSS stations. We find that while the SDOE correction works fairly well for some pixels, the MPOE correction grid produces better results overall (Fig. 4). When we apply the SDOE correction to our InSAR time series, we find that 80% of our 62 comparison pixels' time series still have some residual visible estimated coseismic offset, varying in magnitude from 5 - 36 mm. In addition, at certain station locations, the SDOE correction produces an anomalous coseismic offset. This offset is introduced as an effect of both the noise present in the InSAR data and the fact the SDOE coseismic correction is an exact difference between two time series data points, rather than a difference between model-derived displacements that are estimated from all data points. The pixel at the location of GNSS station P594 illustrates this effect in Fig. 4. Within Fig. 2, we see that, in LOS displacement, the Ridgecrest earthquake caused the location of station P594 to move towards the satellite (a positive offset); yet when we apply the SDOE coseismic correction, the pixel at station P594 shows a residual, negative coseismic offset in the estimated time series (Fig. 4A). This is a consequence of differencing a time series displacement point at the bottom of the pre-earthquake spread of data with a displacement point at the top of the post-earthquake spread, effectively introducing an artificial offset of the approximate size of the spread or noise of the data. The fact that this epoch-to-epoch SDOE approach is so affected by noise indicates that, while it is simple and fast to compute, it is not a feasible method for accomplishing an accurate coseismic displacement estimate in our InSAR time series. By taking the spread of noise into account in our coseismic estimates with the MPOE method however, we are able to more accurately correct the InSAR time series for the Ridgecrest earthquakes offset. This is most visible by directly comparing the InSAR time series for stations P580 and P594 in Figs 4A and 4B (black circles). By applying a more accurate correction, this approach allows us to apply temporal smoothing and the CSS correction with more confidence, now that the sharp, large-magnitude displacements have been removed. We choose to apply this coseismic correction going forward and we refer to this MPOE-corrected data as our "coseismiccorrected" time series. In our coseismic corrected time series set, 24 pixels at GNSS station locations exhibit the behavior similar to that shown by station P580's time series in Fig. 4B, wherein there is a small

310

311

312

313

314

315

316

317

318

319

320

321

322

323

324

325

326

327

328

329

330

331

332

333

334

335

336

337

338

339

amount of apparent coseismic offset still fit by the time series model after the coseismic correction is applied. Fifteen (24%) of these 62 pixels show post-correction coseismic offsets of 5 - 14 mm, while the rest show offsets less than 5 mm. Our MPOE correction method reduces the conspicuous artificial offset present in the SBAS-based coseismic corrected time series (MPOE produces 7 mm, while the SDOE coseismic correction produces 21 mm leftover offset), but does not fully capture and remove it. We attribute this leftover coseismic displacements at these pixel locations to the high noise levels present in the InSAR time series data, and in the Discussion section we explore a further GNSS-based correction step that helps alleviate this issue (see section 4.2). In principle, when we remove the conspicuous coseismic displacements, the leftover earthquakerelated deformation is due to postseismic processes. Previous assessments of GNSS motions have resulted in estimates of cumulative postseismic motion up to tens of millimeters near the earthquake area (Brooks et al. 2020; Floyd et al. 2020), which are in reasonable agreement with those measured by Wang & Bürgmann (2020) from InSAR measurements and by Golriz et al. (2021) from high-rate GNSS displacements. Due to the relatively small amounts of postseismic displacements over the scene, we choose to apply the CSS (Tymofyeyeva & Fialko, 2015)

have resulted in estimates of cumulative postseismic motion up to tens of millimeters near the earthquake area (Brooks *et al.* 2020; Floyd *et al.* 2020), which are in reasonable agreement with those measured by Wang & Bürgmann (2020) from InSAR measurements and by Golriz et al. (2021) from high-rate GNSS displacements. Due to the relatively small amounts of postseismic displacements over the scene, we choose to apply the CSS (Tymofyeyeva & Fialko, 2015) correction to our coseismic-corrected time series. We seek to assess whether we achieve reasonable results with this method, despite the fact that the surface is experiencing non-steady-state motions. In order to reduce the noise level caused by atmospheric effects, we choose to run these new coseismic-corrected time series through SBAS using a subjective temporal smoothing factor of one and a three-iteration CSS correction (Tymofyeyeva & Fialko, 2015). The temporal smoothing factor (Schmidt & Bürgmann, 2003) helps control large changes from epoch to epoch in the time series (with a factor of zero providing no smoothing and a value of 10 for example, causing strong smoothing), while the CSS correction helps correct for propagation delays through the troposphere and the ionosphere using an iterative procedure (Tymofyeyeva & Fialko, 2015, see their Section 2; Xu *et al.* 2017). Multiple iterations are recommended for the CSS correction to be most effective (Tymofyeyeva & Fialko, 2015), and we choose three iterations here to balance computation time efficiency and effectiveness. Results of this processing are presented in Fig. 4C.

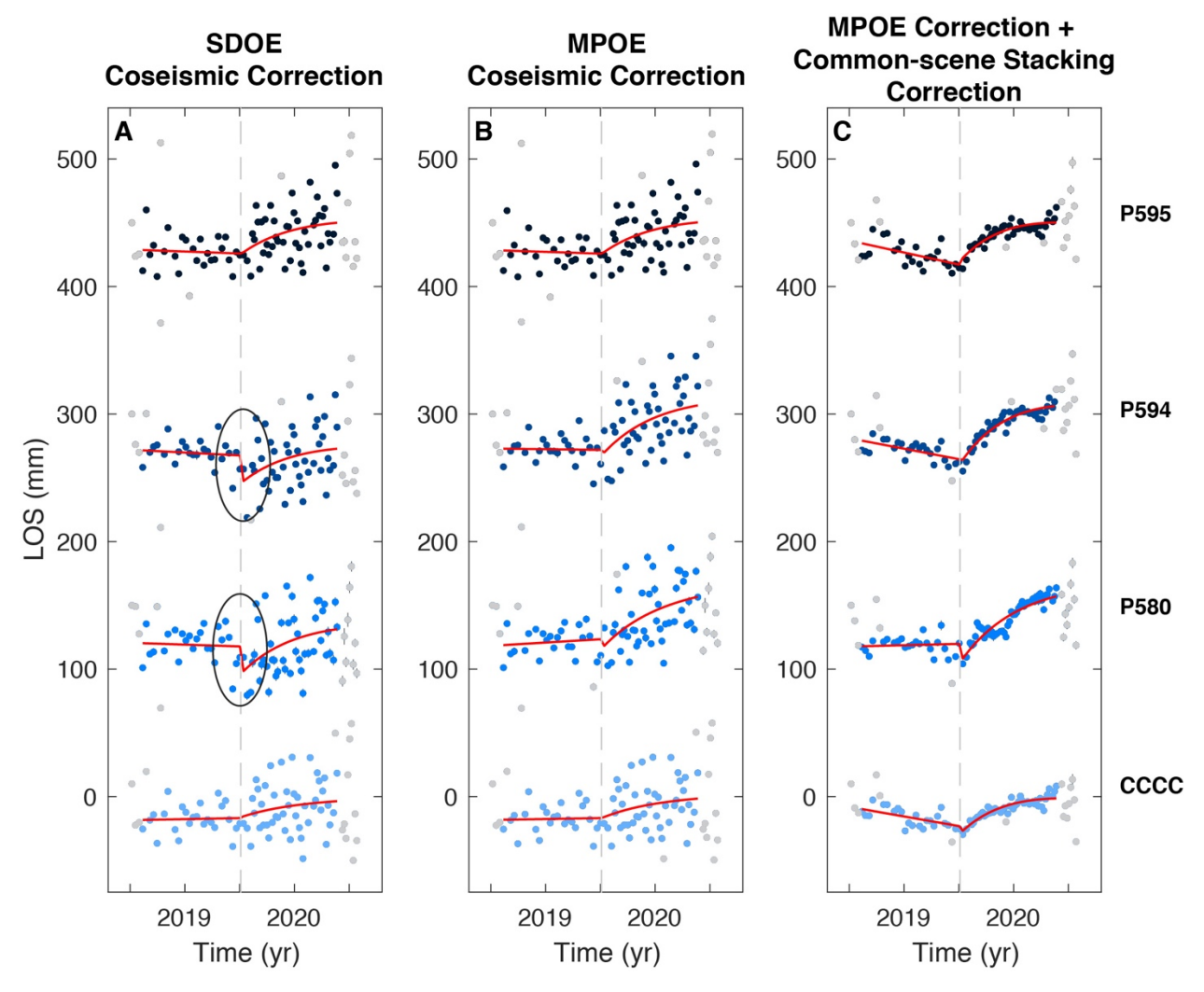


Figure 4. Results of our two coseismic correction methodologies on four pixels of our descending track InSAR time series; (A) shows the Simple Difference Offset Estimate (SDOE) correction, (B) shows the Multiparameter Offset Estimate (MPOE) correction, and (C) shows the MPOE correction in combination with the CSS atmospheric correction. Red lines are the respective estimated time series models. Grey points in the InSAR time series are points that have been removed before model estimation analysis.

For all our SBAS-produced InSAR time series, we trim off three points at the beginnings and nine points at the ends of the time series data (**Fig. 4**). This is due to the fact that the CSS noise estimate depends on having data on both sides of any given time epoch. Thus, at the beginning and end of the series, there is not a lengthy enough dataset on the given side to achieve an accurate result. We then apply a check for conspicuous outliers, using a 25-point (epoch) mean moving window, which will reject points that are more than three standard deviations away from the mean of a 25-point set. For a 6 - 12 day repeat time, this equates to a window of 72 - 300

days. We chose this window as it was the minimum one we tested that removed the most visually conspicuous outliers in the time series. This generally removes up to 1 - 3 data points in each time series. Once outliers and ends are removed, we estimate our time series model as described in Section 2.4. In doing so, we estimate varying amounts of postseismic motion for different stations over the first two months after the events, ranging from 3.9 - 14.3 mm for our coseismic-corrected time series, and 3.5 - 24.3 mm for our coseismic-corrected and CSS-corrected time series at GNSS station positions nearest to the event (**Table 1**). Plotted estimates of cumulative postseismic deformation are presented as interpolated surfaces in **Fig. 5** (a comparison between the descending track and ascending track estimates is presented in **Fig. S3**).

The estimated postseismic displacements measured in our InSAR time series are in general much larger than those measured with GNSS instruments (two to seven times larger for the stations presented in **Fig. 4**). We further discuss, investigate, and reduce this discrepancy in the next section.

Table 1. Estimated cumulative postseismic deformation in a 48-day period for ten GNSS station locations in our InSAR time series datasets, as compared to that estimated from Wang & Bürgmann (2020).

Ctation	Location		Cumulative Postsiesmic (48								
Station	Location		days) This Study†							Wang & Bürgmann (2020)	
	Longitude	Latitude	InSAR (CC)*	InSAR (CC+AC)*	GNSS*	GNSS ± 1σ	GNSS- Cor** InSAR (CC)	GNSS- Cor** InSAR (CC+AC)	InSAR §	GNSS §	
	(°W)	(°N)		(mm)	(mm)	(mm)	(mm)	(mm)	(mm)	(mm)	
BEPK	-118.07409	35.87839	14.33	11.70	-2.33 ± 0.40	-1.22 ± 0.32	-2.67	-1.18	-	-	
										-3 — -	
CCCC	-117.67117	35.56531	3.92	6.62	-0.71 ± 0.34	0.39 ± 0.28	0.64	0.54	~ 3.0	4	
GOL2	-116.88925	35.42516	8.07	3.55	1.35 ± 0.36	2.59 ± 0.31	2.22	1.22	-	-	
ISLK	-118.47430	35.66227	13.66	24.31	-0.01 ± 0.46	0.80 ± 0.41	1.03	2.73	-	-	
P569	-118.12377	35.37797	10.46	11.85	-0.36 ± 0.37	0.71 ± 0.34	1.39	0.78	-	-	
P570	-118.26004	35.66735	10.56	19.87	-1.09 ± 0.34	0.08 ± 0.25	0.62	2.09	-	-	
P580	-117.19223	35.62095	10.13	7.63	2.74 ± 0.28	3.72 ± 0.25	3.36	3.74	-	-	
									12.5 -		
P594	-117.39013	35.89671	11.25	8.28	3.92 ± 0.57	6.14 ± 0.52	5.38	5.20	14	~ 4	
P595	-117.40284	35.69756	7.62	7.01	2.51 ± 0.29	3.68 ± 0.26	3.86	3.14	~3.0	3 - 4	

P597	-116.88840	35.71060	9.25	3.49	1.93 ± 0.30	2.99 ± 0.26	1.73	1.33	_	-	
† Using an exponential function with a tau term of 0.5 yr (182.5 days)											
* Time Series referenced to the location of station HCMN											
CC = MPOE Coseismic Correction applied											
AC = Common-scene Stacking Atmospheric Correction applied											
** Flevation Dependent Atmospheric Correction applied											

 $\$ Values extracted from Wang & Bürgmann (2020) figure 7b 402

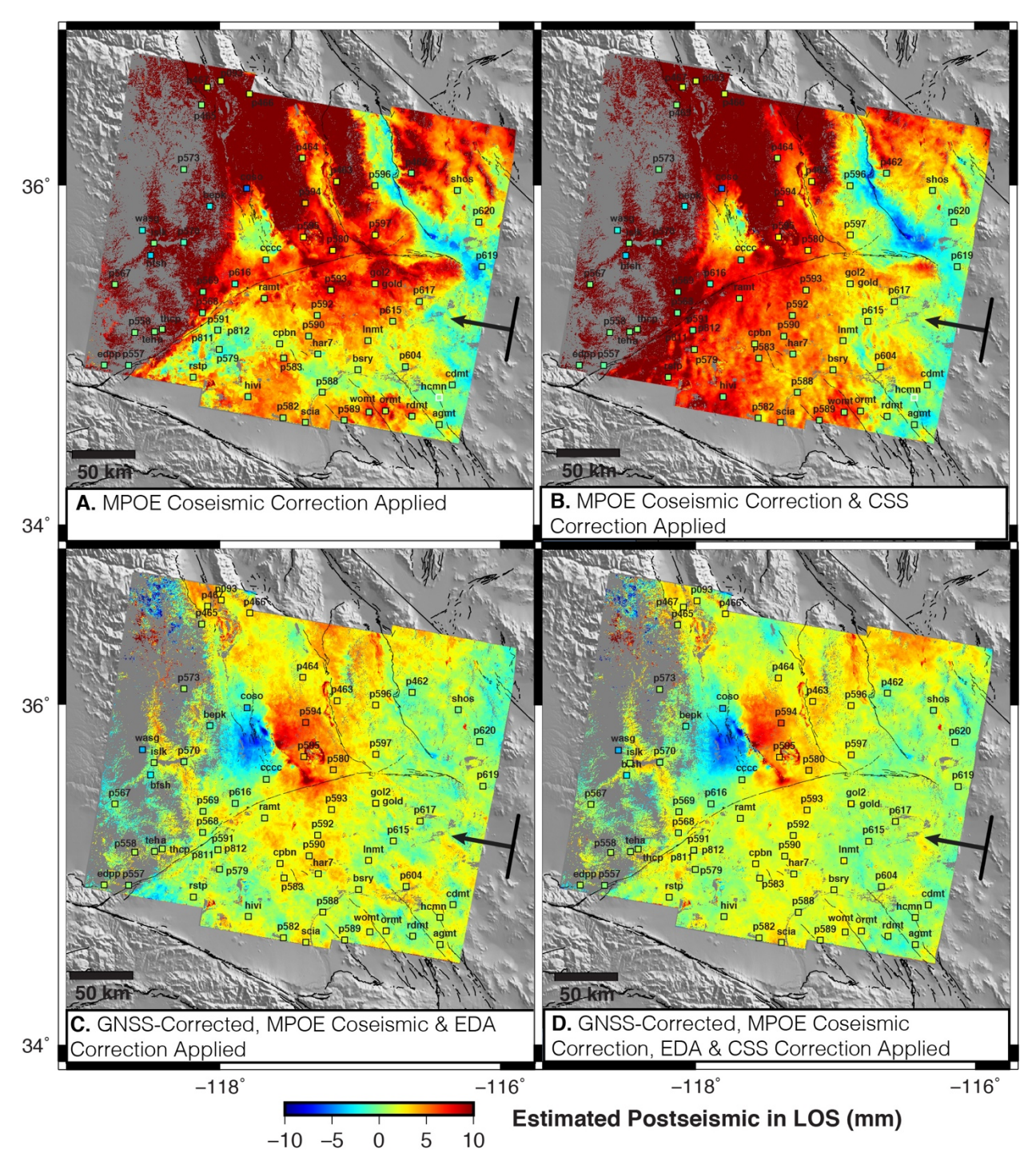


Figure 5. Postseismic displacements estimated from sets of InSAR time series for the 48-day period following the event (July 5th to August 21st); (A) Estimated from our coseismic corrected InSAR time series; (B) Estimated from our coseismic-corrected InSAR time series, with the additional Common-scene Stacking (CSS) correction, (C) Estimated from our GNSS-Corrected, Elevation Dependent Atmospheric (EDA) correction-corrected, coseismic-corrected InSAR time series, and (D) Estimated from the same GNSS- and EDA correction-corrected InSAR time series with the additional CSS correction. All labeled

squares show the magnitude of postseismic displacements estimated from the GNSS time series. White outlined square in (A,B) is the reference point for non-GNSS-corrected InSAR time series (bottom right of (A,B)), labeled HCMN. 3.1 Improved Isolation of the Postseismic Signal In removing the coseismic offset from our InSAR time series, we have produced a dataset that can undergo temporal smoothing and a CSS atmospheric correction within the SBAS program. The discrepancy noted between estimates of postseismic deformation from our InSAR and GNSS time series, however, motivates us to investigate how we can achieve more consistent estimated results between these two datasets. Accurately estimating the magnitude of postseismic deformation following a large earthquake is crucial given that these estimates inform modeling efforts to piece apart mechanisms of postseismic deformation and determine possible stressbased effects on nearby faults. In theory, InSAR measurements of ground motion in the LOS direction should match the GNSS measurements of ground motion projected into LOS, assuming that they are observing the same processes at the surface, particularly earthquake related processes. If these measurements are a poor match to each other, one of the main explanations is that InSAR is known to contain many sources of noise, including spatially and temporally dependent tropospheric, ionospheric, decorrelation and topographic effects, as well as processing-based phase unwrapping errors (Chen & Zebker, 2014; Fattahi & Amelung, 2015; Liu et al. 2014; Zebker et al. 1997; Zebker & Villasenor, 1992). GNSS motions, on the other hand, have many of these types of errors accounted for and corrected during processing. Furthermore, GNSS measurements can provide an "absolute" (global) reference system for InSAR measurements. Therefore, if we correct our InSAR data using GNSS motions, we can achieve a more accurate integrated LOS time series product (Neely et al. 2020; Xu et al. 2021). In the following section, we use this approach to

produce an integrated time series product that takes into account the Ridgecrest earthquake

3.1.1 Correcting InSAR with Continuous GNSS Motions

offsets and provides an improved estimate of postseismic deformation.

410

411

412

413

414

415

416

417

418

419

420

421

422

423

424

425

426

427

428

429

430

431

432

433

434

435

436

437

438

To correct our descending and ascending track InSAR interferograms using continuous GNSS daily displacements, we first downsample our daily GNSS time series to a weekly format (Klein et al. 2019) to suppress the scatters in daily solutions (considering the 6-day minimal repeat of Sentinel-1). To do so, we apply a median filter on the weekly data to ensure only representative motions are included. In the special case of the Ridgecrest earthquake sequence, which occurred midweek, we break up a single week into "pre-Ridgecrest earthquake" and "post-Ridgecrest earthquake" partial weeks of four and three days respectively, to ensure we do not smooth over the coseismic displacements. Once the GNSS weekly dataset is prepared, we begin by applying a combination of the methodologies of Argus et al. (2005), Neely et al. (2020) and Xu et al. (2021). This GNSScorrection process is described in detail in the methods section of Xu et al. (2021), and we describe here how we deviate from their process. We begin by applying an Elevation Dependent Atmospheric (EDA) phase correction to all non-Ridgecrest earthquake spanning interferograms, in order to help correct for topographically correlated atmospheric path delays (Elliott et al. 2008). This assumes a linear relationship between path delay and height, which has been shown by Elliott et al. (2008) to be a reasonable approximation. To start with, we do not apply the EDA correction to the earthquake spanning interferograms due to the large amount of coseismic deformation present in each interferogram. Once the EDA correction has been applied, we calculate the GNSS displacements in LOS using all three GNSS components for all interferogram pairs, and then calculate the residuals (InSAR - GNSS) between the InSAR and GNSS displacements (See Fig. S4 for visual examples). A script that accomplishes this correction is included in the most recent GMTSAR version 6.1 software distribution (correct insar with gnss.csh, GMTSAR GitHub: https://github.com/gmtsar/gmtsar). This correction does not currently take GNSS uncertainties (in particular, larger vertical uncertainties) into account. We then apply a Gaussian filter with a wavelength of 40 km, which is the average distance between our GNSS stations, to the interpolated residual surface, and subtract that final interpolated, filtered surface from the InSAR interferogram. With our new set of GNSS-corrected interferograms, we apply SBAS to calculate our deformation time series in the same way as before. First, we run SBAS with all interferograms

440

441

442

443

444

445

446

447

448

449

450

451

452

453

454

455

456

457

458

459

460

461

462

463

464

465

466

467

468

469

with no additional smoothing and no CSS correction. This set includes the Ridgecrest earthquake offset (**Fig. 6A**; **Fig. S5**). We then calculate our MPOE coseismic correction grid, and remove it from our ten earthquake-spanning GNSS-corrected interferograms. At this point, now that the coseismic deformation is removed, we then apply the EDA correction to these specific earthquake-spanning interferograms and run a second SBAS with no additional smoothing and no CSS correction to assess the results of the coseismic correction (**Fig. 6B**; **Fig. S6**). Lastly, we run a third SBAS that includes the CSS correction (Tymofyeyeva & Fialko, 2015) and a temporal smoothing parameter (Schmidt & Bürgmann, 2003) to produce the final results presented in **Fig. 6C** (**Fig. S7**). This newly created InSAR time series dataset more closely matches the weekly GNSS time series observations. **Fig. S8** illustrates the same effects for the ascending InSAR time series dataset.

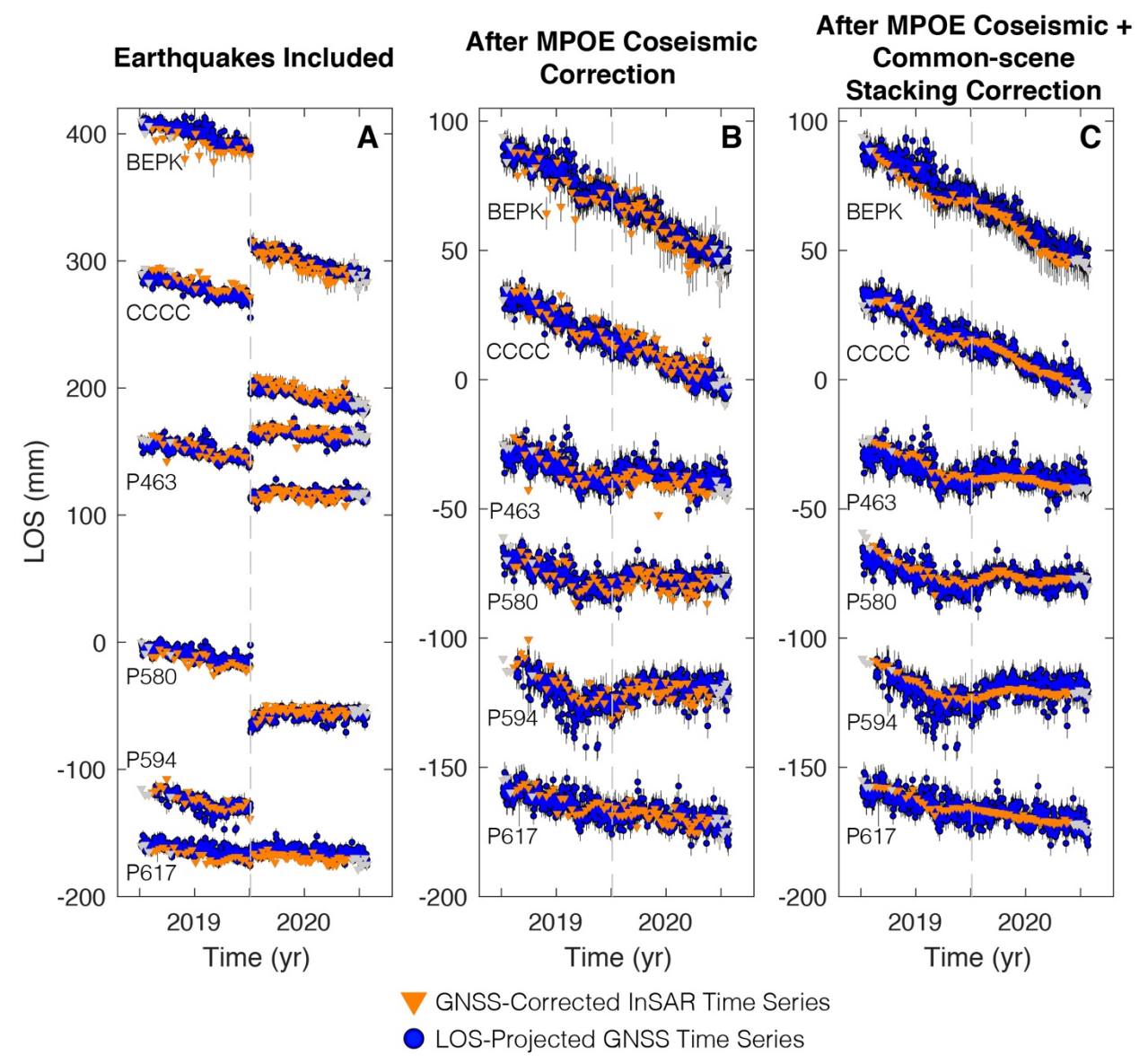


Figure 6. Descending track 71 GNSS-corrected InSAR time series plotted on top of GNSS time series in three cases; (A) Time series including the earthquakes' offset (with an Elevation Dependent Atmospheric (EDA) Correction applied to all but coseismic interferograms); (B) Results of applying our MPOE coseismic correction with an EDA correction for all interferograms and (C) Results of applying the CSS atmospheric correction. Note scale on panel A has a larger LOS range for display purposes. See **Fig. S7** for the ascending track version.

3.2 Results of Postseismic Estimates from GNSS-Corrected InSAR Time Series

When we calculate estimated postseismic displacements from these GNSS-corrected and MPOE coseismic-corrected InSAR time series, we find that they match those estimated from GNSS time

series much more closely, with 82% of stations matching within 2σ uncertainties of GNSS estimates (92% within 3σ uncertainties of GNSS estimates). The comparison of **Fig. 5A** and **Fig. 5C** visually illustrates the amount of improvement between postseismic estimates for a 48-day period. In **Fig. 5C**, the background surface from our InSAR multiparameter estimate grid matches the GNSS postseismic deformation estimates (plotted as squares) much better than the postseismic surface estimated from our coseismic corrected InSAR time series that does not have the GNSS or EDA correction (**Fig. 5A**), particularly on the western (far-range) side of the scene. **Table 1** presents the estimated values of postseismic displacement derived from InSAR time series for ten station locations nearest to the earthquake event. **Figure 7** illustrates a direct scatterplot comparison for all 62 station locations' interseismic, coseismic and postseismic estimates.

In addition, when we assess the performance of our MPOE coseismic correction on the descending track GNSS-corrected time series, we find that any leftover estimated coseismic displacement is < 2 mm, with only 11 stations presenting between >1 mm of displacement. This indicates that the GNSS data-based correction reduces the levels of noise in the data, enabling us to achieve a more accurate coseismic correction for all stations (**Fig. 7B**). In the ascending track, only 15 of 64 stations show leftover estimated coseismic displacements that are > 2 mm, with all but two of those stations exhibiting 2 - 4 mm of leftover displacement.

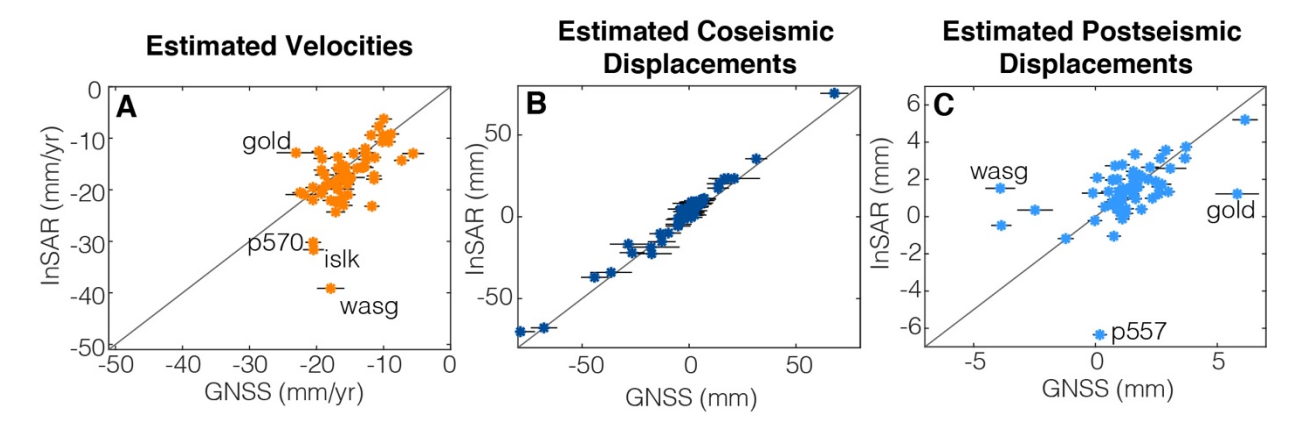


Figure 7. Scatterplot comparison of time series model parameters estimated from GNSS time series for 62 stations (plotted with their formal one-sigma uncertainties) and our descending track GNSS-corrected InSAR time series for the same pixel locations, plotted on top of a line with a slope of one; (A) shows estimated velocity values, (B) shows estimated coseismic displacements and (C) shows estimated

cumulative postseismic displacements for a 48-day period following the earthquake. We label the largest outlier GNSS stations (see section 3.3.1 for discussion).

3.3 InSAR Time Series-derived Earthquake Cycle Products

An added benefit of calculating a MPOE coseismic estimate method is that we can also solve for other time series parameters for every pixel across the InSAR scene, including both postseismic displacements and interseismic velocity. This method produces **Fig. 8**, which illustrates the multiparameter estimates of interseismic velocity, coseismic displacement and the amount of cumulative postseismic displacements estimated over a 48-day period following the earthquake.

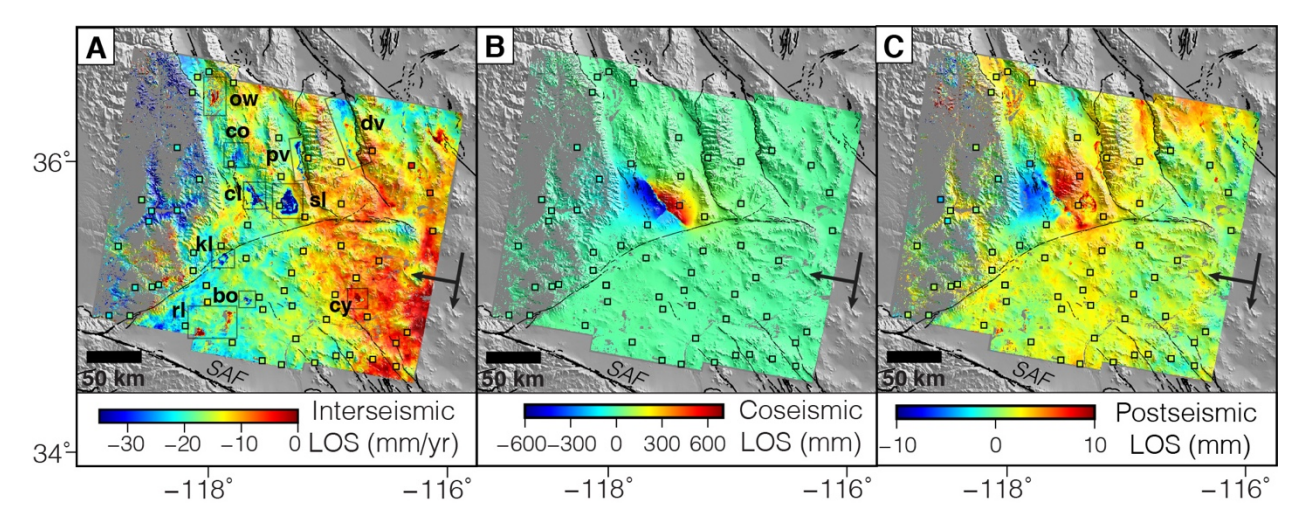


Figure 8. Estimated earthquake cycle grids derived from our GNSS-corrected, coseismic-corrected, EDA-corrected and CSS-corrected InSAR time series, overlaid on topography, with areas <0.45 coherence masked out; (A) shows the estimated interseismic velocity field with highlighted areas of subsidence or uplift, (B) shows the estimated coseismic displacement and (C) shows the cumulative estimated postseismic displacements for a 48-day period following the event (or $D_{postseismic}(t)$ in [3]). Squares are locations of GNSS stations, with the equivalent values estimated from GNSS time series. Note changes in scales between panels. Abbreviations are bo = Borax Mine, cl = China Lake, co = Coso Volcanic Field, cy = Coyote dry lake, dv = Death Valley, kl = Koehn Lake, ow = Owens Lake, pv = Panamint Valley, rl = Rosamund and Rodgers dry lakes, SAF = San Andreas Fault, and sl = Searles Lake.

In our two-year interseismic velocity estimate grid, we can see a gradient of surface motion away from the satellite increasing towards the northwest. We also observe the effects of subsidence occurring at Searles Lake (largest blue feature in center of Fig. 8A), China Lake (labeled box to

the northwest), Coso Volcanic field (box to the north), the dry lakebed in the southern Panamint Valley near Ballarat (box to the northeast of Searles Lake), Koehn Lake (box located in the stepover of the Garlock Fault to the southwest) and the Borax mining activity occurring north of Boron, CA (small box labeled "bo"). In addition, we can see possible uplift around the desert lakebeds of Rosamund dry lake, Rogers dry lake in the western Mojave, Coyote dry late in the eastern Mojave, and Owens Lake near Lone Pine in the Owens Valley to the northwest. In Death Valley, we can see signals of both uplift and subsidence in different areas of Badwater Basin.

Estimating 48 days of cumulative postseismic displacement with our multiparameter method results in an image (**Fig. 8C**) that shows the expected postseismic motions with respect to the descending satellite along both the M_W 6.4 and M_W 7.1 rupture zones, and highlights areas of potential afterslip or poroelastic rebound along the M_W 7.1 rupture zone. Our estimated result agrees fairly well with the descending track postseismic interferogram presented by Wang & Bürgmann (2020) (see their Figure 7b) near the rupture area, and both identify the largest area of postseismic slip to be near the epicenter of the M_W 7.1 event. Analysis of the exact mechanisms of this postseismic deformation is beyond the scope of this study, but is an active area of research (e.g., Wang *et al.* 2021).

By using a multiparameter method to estimate the postseismic amplitude from our full GNSS-corrected InSAR time series, we can use this amplitude grid to calculate a cumulative postseismic displacement grid over any given time period (**Fig S9**). To do this, one needs to assume (1) the postseismic deformation from the event is best fit by a chosen postseismic function (the one used to estimate the amplitude), and (2) the characteristic relaxation time (τ), is constant over both time and space. These assumptions are not necessarily valid, given that best fit tau relaxation times can vary across time (e.g., Jiang *et al.* 2021) and space (e.g., Sobrero *et al.*, 2020), and different postseismic functions (with single or multiple terms) may be needed to describe the full postseismic signals produced by an earthquake (e.g., afterslip, poroelastic effects and/or viscoelastic relaxation, depending on the event). In the case of the Ridgecrest event, we use an exponential function to describe the postseismic deformation as in [1] and [2]:

$$D_{postseismic}(t) = Amplitude * \left(1 - e^{-\frac{\Delta t}{\tau}}\right)$$
 [3]

574 575 where amplitude is estimated during the least-squares inversion described in **Section 2.3.2**. In 576 using our chosen constant relaxation time tau = 0.5 year and an arbitrary 48-day time window 577 $(\Delta t = 0.131 \text{ year})$, we can use the known, calculated grid of postseismic amplitude values to 578 calculate the cumulative postseismic displacements (Fig. 8C), as estimated from the InSAR time 579 series. This process allows us to calculate an InSAR-derived postseismic grid product for any 580 given postseismic time window after the earthquake (Fig. S9), as long as the above assumptions 581 are maintained. The earliest postseismic motions (e.g., Golriz et al. 2021) likely will be included 582 in the coseismic estimate from the InSAR data due to the unavoidable time constraint of the 583 twelve-day data collection window; however, addressing this issue is an active area of research. 584 585 3.3.1 A Note on Matching InSAR with GNSS 586 During our analysis of the descending GNSS-corrected InSAR time series, we observe that 587 stations ISLK, GOLD, P093, P465, P466, P467, P557, P558, P570, p620, SHOS, and WASG 588 produce InSAR time series that do not match the GNSS time series well (Fig. S10). In particular 589 their estimated long-term velocity trends exhibit a discrepancy of 7 - 33 mm/yr, depending on the 590 station. These stations either lie in areas of poor coherence or on the edges or corners of the 591 processed interferogram and therefore may have phase unwrapping errors or InSAR time series 592 that cannot be properly calculated through the SBAS process, without additional data on all sides 593 of the study area. Additionally, stations like GOLD and P557 have substantial (4-9 months-long) 594 gaps in their GNSS time series which can affect both the GNSS correction of the InSAR 595 interferograms, as well as the estimation of time series parameters. In many of these cases, we 596 expect that with longer time series these velocity trend mismatches will be reduced. 597 598 One difference between how we estimate time series model parameters between InSAR and 599 GNSS is that we choose not to estimate seasonal terms for our two-year GNSS-corrected InSAR 600 displacement time series model fits, as mentioned in section 2.3.2. This may introduce a source 601 of epistemic uncertainty when we then compare the results to GNSS time series models that have 602 had annual and semi-annual seasonal terms estimated. To illustrate the effect of not estimating 603 seasonal terms on our two-year InSAR time series, we plot six example location time series

residuals in Fig. S11, showing what the time series look like (Fig. 11A), what the residuals look

like without seasonal terms estimated (**Fig. 11B**) and what they look like with seasonal terms estimated (**Fig. 11C**). To create this plot, we estimate an annual and semi-annual set of terms in the same manner as we do for GNSS time series model fits (eqn. [1]). Seasonal signals can be visually identified in our residuals, though we suggest that these signals are best recovered with a longer span of time series than the two years we analyze here. In addition, we show what differences occur in our interseismic and postseismic multiparameter estimate grids when seasonal terms are estimated (**Fig. S12**). While there are no extreme differences, it appears as though estimating seasonal terms increases the amplitude of the interseismic and postseismic signals in certain areas across the scene, indicating that certain tradeoffs are occurring during the time series inversions. More investigation, with a longer time series, is needed to best isolate the postseismic signal from the other signals present in the time series.

4. Conclusion

The spatial resolution of InSAR displacement time series enables us to investigate many time-dependent Earth processes in more detail than provided by individual interferogram pairs. When using InSAR time series, however, common processing algorithms to reduce noise call for an assumption of steady deformation through time, which becomes problematic when earthquakes occur. In order to correct a sharp coseismic step introduced by an earthquake, we test two methods that seek to remove the coseismic offset from InSAR time series: (1) a Simple Difference Offset Estimate (SDOE) correction and (2) a Multiparameter Offset Estimate (MPOE) time series inversion coseismic estimate correction. We apply these two methods to time series surrounding the 2019 Ridgecrest earthquake sequence and find that the MPOE coseismic correction more accurately corrects for coseismic displacements, as it can account for noise present in the InSAR time series in a way that the SDOE correction cannot. Using this correction produces an InSAR time series that can successfully undergo the application of smoothing constraints as well as the CSS atmospheric correction.

To improve upon estimates of postseismic deformation from our InSAR time series, we employ weekly GNSS displacement time series (Klein *et al.* 2019) to correct our interferograms (Neely *et al.* 2020; Xu *et al.* 2021). Including LOS-projected GNSS displacements allows us to correct for additional atmospheric signals in the interferogram and to provide an underlying frame of

636 reference for the InSAR interferograms. This results in GNSS-corrected InSAR interferograms 637 and time series, which produce more realistic estimates of postseismic deformation following the 638 Ridgecrest earthquake sequence than does our non-GNSS corrected InSAR time series. We 639 provide our two-year, GNSS-corrected, coseismic-corrected and EDA-corrected descending and 640 ascending track InSAR time series displacements for GNSS station locations near the Ridgecrest 641 earthquake (Data File S1, S2), as well as a set that have been corrected with the CSS correction 642 (Data File S3, S4). 643 644 The use of a multiparameter estimation approach also enables us to produce GNSS-corrected 645 InSAR data-derived estimates of interseismic, coseismic, and postseismic deformation, all in grid 646 format. We show that model-based postseismic deformation grids can be successfully estimated 647 from the InSAR time series for any time interval using an exponential postseismic model and a 648 multiparameter time series approach. Having an InSAR data-derived earthquake cycle product 649 will facilitate further characterization of the mechanisms of postseismic deformation following 650 the Ridgecrest event and help to discern which mechanisms (e.g., afterslip, poroelastic effects, 651 viscous relaxation) dominate. 652 653 5. Acknowledgements 654 We thank Chris Rollins and an anonymous reviewer for their thoughtful and detailed comments 655 and suggestions, which greatly improved this manuscript. This study was partly funded by the 656 NASA Earth Surface and Interior Program (80NSSC19K1043), the National Science 657 Foundation, Office of Advanced Cyberinfrastructure (OAC-1834807), and the Southern 658 California Earthquake Center (SCEC) (20074). This research was also supported Caltrans 659 Agreement # 52A0128. GNSS Displacement time series processing and research is funded by 660 NASA NNH17ZDA001N-MEASURES. 661 662 **6. Author Contribution Statement** 663 K. Guns completed the InSAR time series processing and main analysis, with supervisory 664 assistance from both X. Xu and D. Sandwell. X. Xu and D. Sandwell wrote the main code for the 665 GNSS-correction processing. Y. Bock supervised the production of the GNSS displacement time 666 series and performed quality control with K. Guns. K. Guns completed the GNSS-correction

- application processing, with supervisory assistance from X. Xu, D. Sandwell, and Y. Bock. K.
- 668 Guns wrote this paper with editorial and substantive changes from X. Xu, D. Sandwell, and Y.
- 669 Bock.

- 7. Data Availability Statement: All Sentinel-1 InSAR raw SLC data processed and presented in
- this study are freely available from the Alaska Satellite Facility (https://search.asf.alaska.edu/#/)
- and all GMTSAR processing programs and scripts are freely available on Github
- 674 (https://github.com/gmtsar/gmtsar). All processed GNSS data used in this study are freely
- available on a weekly basis as explained at the Scripps Orbit and Permanent Array Center
- 676 (SOPAC) MEaSUREs products page (http://sopac-csrc.ucsd.edu/index.php/displacements/).

677

- **8. References**
- Agram, P.S., & Zebker H.A., 2009. Sparse Two-Dimensional Phase Unwrapping Using Regular-
- 680 Grid Methods, IEEE Trans. Geosci. Remote Sens. Lett., 6(2), 327 331.
- 681 https://doi.org/10.1109/LGRS.2009.2012445.

682

- Argus D.F., Heflin, M.B., Peltzer, G., Crampé, F., & Webb, F.H., 2005. Interseismic strain
- accumulation and anthropogenic motion in metropolitan Los Angeles, *Journal of Geophysical*
- 685 Research, 110, B04401. https://doi.org/10.1029/2003JB002934

686

- Bekaert, D.P.S., Handwerger, A.L., Agram, P., & Kirschbaum, D.B., 2020. InSAR-based
- detection method for mapping and monitoring slow-moving landslides in remote regions with
- steep and mountainous terrain: An application to Nepal, *Remote Sensing of Environment*, 249.
- 690 https://doi.org/10.1016/j.rse.2020.111983

691

- 692 Berardino, P., Fornaro, G., Lanari, R., & Sansosti, E., 2002. A New Algorithm for Surface
- 693 Deformation Monitoring Based on Small Baseline Differential SAR Interferograms, *IEEE Trans*.
- 694 *Geosci. Remote Sens.*, 40, 11, 2375 -- 2383. https://doi.org/10.1109/TGRS.2002.803792

695

- Biggs, J. & Wright, T.J., 2020. How satellite InSAR has grown from opportunistic science to
- routine monitoring over the last decade, *Nature Communications*.
- 698 https://doi.org/10.1038/s41467-020-17587-6

699

- Bevis, M. and Brown, A., 2014. Trajectory models and reference frames for crustal motion
- 701 geodesy, *Journal of Geodesy*, 88, 283 -- 311. <u>https://doi.org/10.1007/s00190-013-0685-5</u>

702

- Bock, Y. & Melgar, D., 2016. Physical Applications of GPS Geodesy: A Review, Rep. Prog.
- 704 *Phys.* 79, 10. <u>https://doi.org/10.1088/0034-4885/79/10/106801</u>

- Bock, Y. & Wdowinski, S., 2021. GNSS Geodesy in Geophysics, Natural Hazards, Climate, and
- the Environment, in Position, Navigation, and Timing Technologies in the 21st Century:

- 708 Integrated Satellite Navigation, Sensor Systems, and Civil Applications, *IEEE Trans. Geosci.*
- 709 Remote Sens., 2021, 741 -- 820. https://doi.org/10.1002/9781119458449.ch28

- 711 Bock, Y., Fang, P., Knox, A., Sullivan, A., Jiang, S., Moore, A., Argus, D., Liu, Z., & Kedar, S.,
- 712 2021. Extended Solid Earth Science ESDR System Algorithm Theoretical Basis Document
- 713 (ATBD), October 11, 2021 MEaSUREs ROSES-17, April 4.
- 714 http://garner.ucsd.edu/pub/measuresESESES products/ATBD/ESESES-ATBD.pdf

715

- Prooks, B.A., Murray, J., Svarc, J., Phillips, E., Turner, R., Murray, M., Ericksen, T., Wang, K.,
- 717 Minson, S., Bürgmann, R., Pollitz, F., Hudnut, K., Nevitt, J., Roeloffs, E., Hernandez, J., &
- Olson, B., 2020. Rapid Geodetic Observations of Spatiotemporally Varying Postseismic
- 719 Deformation Following the Ridgecrest Earthquake Sequence: The U.S., Geological Survey
- 720 Response, Seismol. Res. Lett., 91, 2108 -- 2123. https://doi.org/10.1785/0220200007

721

- Bürgmann, R., Rosen, P., & Fielding, E., 2000. Synthetic Aperture Radar interferometry to
- measure Earth's surface topography and its deformation, Ann. Rev. Earth. planet. Sci., 28, 169 –
- 724 209, https://doi.org/10.1146/annurev.earth.28.1.169

725

- Bürgmann, R. Hilley, G., Ferretti, A., & Novali, F., 2005. Resolving vertical tectonics in the San
- 727 Francisco Bay Area from permanent scatterer InSAR and GPS analysis, Geology, 34(3), 221-
- 728 224, https://doi.org/10.1130/G22064.1

729

- Bürgmann, R., & Thatcher, W., 2013. Space geodesy: A revolution in crustal deformation
- measurements of tectonic processes, Geological Society of America Special Paper 500, 1 -- 34.
- 732 <u>https://doi.org/10.1130/2013.2500(12)</u>

733

- Chaussard, E., Wdowinski, S., Cabral-Cano, E., & Amelung, F., 2014. Land subsidence in
- central Mexico detected by ALOS InSAR time-series, Remote Sensing of Environment, 140, 94 -
- 736 106. https://doi.org/10.1016/j.rse.2013.08.038

737

- 738 Chen, C.W., & Zebker, H.A., 2002. Phase Unwrapping for Large SAR Interferograms: Statistical
- 739 Segmentation and Generalized Network Models, *IEEE Trans. Geosci. Remote Sens.*, 40(8), 1709
- 740 -- 1719. https://doi.org/10.1109/TGRS.2002.802453

741

- Chen, C.C., & Zebker, H.A., 2014. Reducing Ionospheric Effects in InSAR Data Using Accurate
- 743 Coregistration, *IEEE Trans. Geosci. Remote Sens.*, 52(1), 60 -- 70.
- 744 https://doi.org/10.1109/TGRS.2012.2236098

745

- Dixon, T., Amelung, F., Ferretti, A., Novali, F., Rocca, F., Dokka, R., Sella, G., Kim, S.-W.,
- 747 Wdowinski, S., & Whitman, D., 2006. Subsidence and flooding in New Orleans, Nature, 441,
- 748 587-588, https://doi.org/10.1038/441587a

749

- 750 Elliott, J.R., Biggs, J., Parsons, B., & Wright, T.J., 2008. InSAR slip rate determination on the
- 751 Altyn Tagh Fault, northern Tibet, in the presence of topographically correlated atmospheric
- delays, Geophys. Res. Lett., 35. https://doi.org/10.1029/2008GL033659

- Fattahi, H., & Amelung, F., 2015. InSAR bias and uncertainty due to the systematic and
- stochastic tropospheric delay, J. Geophys. Res. Solid Earth, 120, 8758 -- 8773.
- 756 https://doi.org/10.1002/2015JB012419

- 758 Fattahi, H., & Amelung, F., 2016. InSAR observations of strain accumulation and fault creep
- along the Chaman Fault system, Pakistan and Afghanistan. Geophys. Res. Let., 43(16), 8399-
- 760 8406. https://doi.org/10.1002/2016GL070121

761

- Floyd, M., Funning, G., Fialko, Y., Terry, R., & Herring, T., 2020. Survey and Continuous
- GNSS in the Vicinity of the July 2019 Ridgecrest Earthquakes, Seismol. Res. Lett., 91 (4): 2047–
- 764 2054. https://doi.org/10.1785/0220190324

765

- Golriz, D, Bock, Y. & Xu, X., 2021. Defining the Coseismic Phase of the Crustal Deformation
- 767 Cycle with Seismogeodesy, J. Geophys. Res. Solid Earth, 126(10), e2021JB022002,
- 768 https://doi.org/10.1029/2021JB022002

769

- Grandin, R., Vallée, M., Lacassin, R., 2017. Rupture process of the M_w 5.8 Pawnee, Oklahoma,
- earthquake from Sentine 11 In SAR and seismological data, Seismol. Res. Lett., 88, 11.

772

- Handwerger, A.L., Huang, M.-H., Fielding, E.J., Booth, A.M., & Bürgmann, R., 2019. A shift
- from drought to extreme rainfall drives a stable landslide to catastrophic failure, *Nature Scientific*
- 775 *Reports*. https://doi.org/10.1038/s41598-018-38300-0

776

- Hardebeck, J., 2020. A Stress-Similarity Triggering Model for Aftershocks of the M_W 6.4 and
- 7.1 Ridgecrest Earthquakes, *Bull. Seismol. Soc. Am.*, 110, 1716 -- 1727.
- 779 https://doi.org/10.1785/0120200015

780

- Hetland, E.A., Musé, P., Simons, M., Lin, Y.N., Agram, P.S., & DiCaprio, C.J., 2012. Multiscale
- InSAR Time Series (MInTS) analysis of surface deformation, J. Geophys. Res., 117, B02404.
- 783 https://doi.org/10.1029/2011JB008731

784

- Hilley, G.E., Bürgman, R., Ferretti, A., Novali, F., & Rocca, F., 2004. Dynamics of Slow-
- moving Landslides from Permanent Scatter Analysis, Science, 304(5679), 1952-1955,
- 787 https://doi.org/10.1126/science.1098821

788

- Hooper, A., Bekaert, D., Spaans, K., & Arlkan, M., 2012. Recent advances in SAR
- interferometry time series analysis for measuring crustal deformation, *Tectonophysics*, 514-517,
- 791 https://doi.org/10.1016/j.tecto.2011.10.013

792

- Hu, X., Bürgmann, R., Schulz, W. H., & Fielding, E. J., 2020. Four-dimensional surface motions
- of the Slumgullion landslide and quantification of hydrometeorological forcing. *Nature*
- 795 Communications, 11(1), 1-9. https://doi.org/10.1038/s41467-020-16617-7

- Hussain, E., Wright, T.J., Walters, R.J., Bekaert, D., Hooper, A., & Houseman, G.A., 2016.
- Geodetic observations of postseismic creep in the decade after the 1999 Izmit earthquake,

- Turkey: Implications for a shallow slip deficit, *J. Geophys. Res. Solid Earth*, 121, 2980 -- 3001. https://doi.org/10.1002/2015JB012737
- 901
- 801
- Jiang, J., Bock, Y., & Klein, E., 2021. Coevolving early afterslip and aftershock signatures of a San Andreas fault rupture, *Sci. Adv.*, 7(15). https://doi.org/10.1126/sciadv.abc1606
- 804
- Jin, Z., & Fialko, Y., 2020. Finite Slip Models of the 2019 Ridgecrest Earthquake Sequence
- 806 Constrained by Space Geodetic Data and Aftershock Locations, Bull. Seismol. Soc. Am., 110,
- 807 1660 -- 1679. https://doi.org/10.1785/0120200060

- Klein, E., Bock, Y., Xu, X., Sandwell, D.T., Golriz, D., Fang, P., & Su, L., 2019. Transient
- Deformation in California from Two Decades of GPS Displacements: Implications for a Three-
- Dimensional Kinematic Reference Frame, J. Geophys. Res. Solid Earth, 124.
- 812 <u>https://doi.org/10.1029/2018JB017201</u>

813

- Liu, F., Elliott, J. R., Craig, T. J., Hooper, A., & Wright, T. J., 2021. Improving the Resolving
- Power of InSAR for Earthquakes Using Time Series: A Case Study in Iran. Geophys. Res. Let.,
- 816 48(14), e2021GL093043. https://doi.org/10.1029/2021GL093043

817

- Liu, Z., Jung, H.-S., & Lu, Z., 2014. Joint Correction of Ionosphere Noise and Orbital Error in L-
- 819 Band SAR Interferometry of Interseismic Deformation in Southern California, *IEEE Trans*.
- 820 Geosci. Remote Sens., 52(6), 3421 -- 3427. https://doi.org/10.1109/TGRS.2013.227.2791

821

- Milliner, C., Donnellan, A., Aati, S., Avouac, J. P., Zinke, R., Dolan, J. F., ... & Bürgmann, R.,
- 823 2021. Bookshelf Kinematics and the Effect of Dilatation on Fault Zone Inelastic Deformation:
- 824 Examples From Optical Image Correlation Measurements of the 2019 Ridgecrest Earthquake
- 825 Sequence. J. Geophys. Res.: Solid Earth, 126(3), e2020JB020551.
- 826 https://doi.org/10.1029/2020JB020551

827

- Neely, W.R., Borsa, A.A., & Silverii, F., 2020. GInSAR: A cGPS Correction for Enhanced
- 829 InSAR Time Series. *IEEE Trans. Geosci. Remote Sens.*, 58(1).
- 830 https://doi.org/10.1109/TGRS.2019.2934118

831

- 832 Neely, W., Borsa, A.A., Burney, J.A., Levy, M.C., Silverii, F., & Sneed, M., 2021.
- 833 Characterization of Groundwater Recharge and Flow in California's San Joaquin Valley From
- 834 InSAR-Observed Surface Deformation, *Water Resources Research*, 57, e2020WR028451.
- 835 https://doi.org/10.1029/2020WR028451

836

- Nikolaidis, R., 2002. Observation of geodetic and seismic deformation with the Global
- 838 <u>Positioning System</u>, PhD Dissertation, University of California, San Diego, La Jolla, California,
- 839 265 pgs.

840

- Plesch, A., Shaw, J.H., Ross, Z.E., & Hauksson, E., 2020. Detailed 3D Fault Representations for
- the 2019 Ridgecrest, California, Earthquake Sequence, Bull. Seismol. Soc. Am., 110, 1818 --
- 843 1831. https://doi.org/10.1785/0120200053

- Poland, M., Bürgmann, R., Dzurisin, D., Lisowski, M., Masterlark, T., Owen, S., & Fink, J.,
- 846 2006. Constraints on the mechanism of long-term steady subsidence at Medicine Lake volcano,
- northern California, from GPS, leveling, and InSAR, J. Volcanology and Geothermal Res., 150,
- 848 55 -78, https://10.1016/j.volgeores.2005.07.007

- Ponti, D.J., Blair, J.L., Rosa, C.M., Thomas, K., Pickering, A.J., Dawson, T.E., 2020. Digital
- datasets documenting surface fault rupture and ground deformation features produced by the
- Ridgecrest M6.4 and M7.1 earthquake sequence of July 4 and 5, 2019, U.S. Geological Survey
- data release, https://doi.org/10.5066/P9BZ5IJ9

854

- Ross, Z.E., Idini, B., Jia, Z., Stephenson, O.L., Zhong, M., Wang, X., Zhan, Z., Simons, M.,
- Fielding, E.J., Yun, S.-H., Hauksson, E., Moore, A.W., Liu, Z., & Jung, J., 2019. Hierarchical
- interlocked orthogonal faulting in the 2019 Ridgecrest earthquake sequence, *Science*, 366, 346 --
- 858 351. https://doi.org/10.1126/science.aaz0109

859

- Sandwell, D. T., Xu, X., Mellors, R., Wei, M., Tong, X., and Wessel, P., 2016. GMTSAR: An
- InSAR Processing System Based on Generic Mapping Tools, Second Ed., available at
- http://topex.ucsd.edu/gmtsar/tar/GMTSAR 2ND TEX.pdf

863

- 864 Schmidt, D.A., & Bürgmann, R., 2003. Time-dependent land uplift and subsidence in the Santa
- 865 Clara valley, California, from a large interferometric synthetic aperture radar data set, J.
- 866 Geophys. Res., 108(B9). https://doi.org/10.1029/2002JB002267

867

- 868 Shirzaei, M., & Bürgmann, R., 2013. Time-dependent model of creep on the Hayward fault from
- joint inversion of 18 years of InSAR and surface creep data. J. Geophys. Res.: Solid Earth,
- 870 118(4), 1733-1746. https://doi.org/10.1002/jgrb.50149

871

- 872 Sobrero, F.S., Bevis, M., Gómez, D.D., & Wang, F., 2020. Logarithmic and exponential
- 873 transients in GNSS trajectory models as indicators of dominant processes in postseismic
- deformation, J. Geodesy. https://doi.org/10.1007/s00190-020-01413-4
- 875 Tong, X., D. T. Sandwell, and B. Smith-Konter, 2013. High-resolution interseismic velocity data
- along the San Andreas Fault from GPS and InSAR, J. Geophys. Res.: Solid Earth, 118.
- 877 https://doi.org/10.1029/2012JB009442
- 878 Tong, X. & Schmidt, D., 2016. Active movement of the Cascade landslide complex in
- Washington from a coherence-based InSAR time series method, *Remote Sensing Environment*,
- 880 186. https://doi.org/10.1016/j.rse.2016.09.008

881

- Tymofyeyeva, E. & Fialko, Y., 2015. Mitigation of atmospheric phase delays in InSAR data,
- with application to the eastern California shear zone, J. Geophys. Res. Solid Earth, 120, 5952 --
- 884 5963. https://doi.org/10.1002/2015JB011886

- Tymofyeyeva, E., Fialko, Y., Jiang, J., Xu, X., Sandwell, D., Bilham, R., ... & Moafipoor, S,
- 2019. Slow slip event on the southern San Andreas Fault triggered by the 2017 Mw 8.2 Chiapas
- 888 (Mexico) earthquake. *J. Geophys. Res.: Solid Earth*, 124(9), 9956-9975.
- 889 https://doi.org/10.1029/2018JB016765

- Wang, K. & Bürgmann, R., 2020. Co- and Early Postseismic Deformation Due to the 2019
- 892 Ridgecrest Earthquake Sequence Constrained by Sentinel-1 and COSMO-SkyMed SAR Data,
- 893 Seismol. Res. Lett., 91(4), 1998–2009. https://doi.org/10.1785/0220190299

894

- Wang, K., Bürgamnn, R., Brooks, B., Svarc, J., Liu, Z., & Fielding, E., 2021. Modeling of
- postseismic deformation following the 2019 Ridgecrest earthquake sequence, Abstract MR31A-
- 897 08 presented at 2021 American Geophysical Union Fall Meeting, New Orleans, LA and Online,
- 898 13-17 Dec.

899

- 900 Wei, S., Fielding, E., Leprince, S., Sladen, A., Avouac, J.-P., Helmberger, D., Hauksson, E.,
- 901 Chu, R., Simons, M., Hudnut, K., Herring, T., & Briggs, R., 2011. Superficial simplicity of the
- 902 2010 El Mayor-Cucapah earthquake of Baja California in Mexico, Nature Geoscience, 4, 615 --
- 903 618. https://doi.org/10.1038/NGEO1213

904

- Weiss J.R., Walters, R.J., Morishita, Y., Wright, T.J., Lazecky, M., Wang, H., Hussain, E.,
- 906 Hooper, A.J., Elliott, J.R., Rollins, C., Yu, C., González, P.J., Spaans, K., Li, Z., & Parsons, B.,
- 907 2020. High-Resolution Surface Velocities and Strain for Anatonia From Sentinel-1 InSAR and
- 908 GNSS Data, Geophy. Res. Lett., 47. https://doi.org/10.1029/2020GL087376

909

- 910 Xu, X., Sandwell, D.T., Tymofyeyeva, E., González-Ortega, A., & Tong, X., 2017. Tectonic and
- Anthropogenic Deformation at the Cerro Prieto Geothermal Step-Over Revealed by Sentinel-1A
- 912 InSAR, *IEEE Trans. Geosci. Remote Sens.*, 55(9), 5284 -- 5292.
- 913 https://doi.org/10.1109/TGRS.2017.2704593

914

- 915 Xu, X., Ward, L. A., Jiang, J., Smith-Konter, B., Tymofyeyeva, E., Lindsey, E. O., ... &
- 916 Sandwell, D. T, 2018. Surface creep rate of the southern San Andreas fault modulated by stress
- 917 perturbations from nearby large events. Geophys. Res. Let., 45(19), 10,259-10,268.
- 918 https://doi.org/10.1029/2018GL080137

919

- 920 Xu, X., Sandwell, D. T., & Smith-Konter, B., 2020b. Coseismic displacements and surface
- fractures from Sentinel-1 InSAR: 2019 Ridgecrest earthquakes. Seis. Res. Let., 91(4), 1979-1985.
- 922 https://doi.org/10.1785/0220190275

923

- Yu, X., Sandwell, D.T., Ward, L.A., Milliner, C.W.D, Smith-Konter, B.R., Fang, P., & Bock, Y.,
- 925 2020a. Surface deformation associated with fractures near the 2019 Ridgecrest earthquake
- 926 sequence, *Science*, 370, 605 -- 608. https://doi.org/10.1126/science.abd1690

927

- 928 Xu, X., Sandwell, D.T., Klein, E., and Bock, Y., 2021. Integrated Sentinel-1 InSAR and GNSS
- 929 time-series along the San Andreas fault system, J. Geophys. Res. Solid Earth, 126(11),
- 930 e2021JB022579, https://doi.org/10.1029/2021JB022579

931

- 200 Zebker, H.A., & Villasenor, J., 1992. Decorrelation in interferometric radar echoes, *IEEE Trans*.
- 933 Geosci. Remote Sens., 30(5), 950-959.

Zebker, H.A., Rosen, P.A., & Hensley, S., 1997. Atmospheric effects in interferometric synthetic aperture radar surface deformation and topographic maps, *J. Geophys. Res.*, 102(B4), 7547 -- 7563.